

APPLICATION OF NUMERICAL METHODS FOR CRASHWORTHINESS INVESTIGATION OF A LARGE AIRCRAFT WING IMPACT WITH A TREE

CHAO ZHANG¹, WIESLAW K. BINIENDA¹, FRANK E. HORVAT², WENZHI WANG³

¹*Department of Civil Engineering, University of Akron, 302 Buchtel Common, Akron, OH, 44325, USA*

²*Department of Mechanical Engineering, University of Akron, 302 Buchtel Common, Akron, OH, 44325, USA*

³*School of Aeronautics, Northwestern Polytechnical University, Xian, Shaanxi 710072, China*

ABSTRACT. This paper demonstrates the application of a numerical methodology for a full-scale aircraft impact crashworthiness investigation. We studied the impact of an aircraft wing with a tree using LS-DYNA and ANSYS CFX. In particular, a detailed finite element model of the wing structure was represented as a box structure containing skin, spars and ribs, and fuel was represented as a distributed mass. We utilized several material models and verified them using leading-edge bird strike and wood bending experiments. Wood model Mat 143 with material parameters developed based on the wood bending test was found to be the most accurate in comparison with the experiment. We used the commercially available Computational Fluid Dynamics (CFD) software of ANSYS CFX to calculate the aerodynamic pressure distribution on the overall surface of the wing. The algorithm utilized the full three-dimensional Navier-Stokes equations for steady-state compressible fluid. LS-DYNA finite element model included aerodynamic pressures on the wings surfaces. Parametric studies showed that the tree model cannot destroy the lifting surface of the wing except the fragment of the leading edge. In every simulation scenario, the first spar of the wing cut through the tree and the upper part of the tree fell in the direction of the movement of the airplane.

Keywords: Full scale modeling, Finite Element Method, crashworthiness, nonlinear wood model, Mat 143, Johnson-Cook material model, fluid dynamics, aircraft, wing, tree.

1 INTRODUCTION

For aircraft crashworthiness analysis, it is important to consider the dynamic behavior of the aircraft under impact conditions. Because impact-related experiments are very difficult to conduct and very expensive, it is of great importance to develop alternative techniques to the experiments, such as analytical and computational methods to obtain an accurate simulation of aircraft structure response to any impact conditions. The finite element explicit codes, such as LS-DYNA, MSC.DYTRAN and PAM-CRASH, are widely used to simulate nonlinear, transient, dynamic events.

There were several studies published on the aftermath of the airplane crashes into the World Trade Center on September 11, 2001. These studies focused on the aluminum wing cutting through the external steel columns of the building, the destruction of the airplane by the building core structure, and the reasons behind the collapse of the skyscrapers. Wierzbicki and Xue [21, 22, 23]

developed analytical and finite element models to study the resistance of the exterior columns, floors and core columns of the building to the impact of the airplane. It was found that the wing of the airplane would easily cut through the outer columns of the building with a cruising speed of 240 m/s. The majority of the kinetic energy (about 50%) was dissipated by the floor, and the remaining plane energy dissipated at the building core columns. Bazant and Zhou [4] estimated that the temperatures in some sections of the building were elevated to 800 °C and 1000 °C due to a fire caused by burning jet fuel. Authors showed that these high temperatures induced the degradation or loss of the load-carrying capability of the steel structure in the floors, which were no longer able to support the weight of the building. Abboud [1] did a simulation study of the whole process – from impact, through the fuel spill and fire, to the collapse of the building using SAP2000 and dynamic nonlinear FLEX. The analysis demonstrated that while the robustness of the tubular-perimeter wall system and the redundancy

of the structure allowed the tower to resist immediate impact damage, the thermal loads overwhelmed the remaining structural system capacity.

On April 10, 2010, a Polish Air Force Tupolev Tu-154M (registration number 101) performing a state flight from Warsaw (Poland) to Smolensk (Russia) crashed into the ground about 500 m short of the runway at Smolensk North Airport (XUBS). [11] reported that the aircraft's left wing was brake off after collision with a birch tree before the crash. However, the role of a tree in breaking the wing is questionable. An analysis of aircraft impact with a tree has only rarely been published. Bocchieri [5] has recently presented a developed simulation of a full-scale experiment involving the crash of a Lockheed Constellation aircraft conducted for the US Department of Transportation. This experiment and simulation studied the process of aircraft wing impact into two telephone poles. The authors of this study used LS-DYNA with Mat143 to simulate the wood material of the poles. All simulations and high-speed video footage of the experiment revealed that the front spar of the wing cut through the telephone poles.

Morka et al. [15] investigated a circular cross-section beam impact with a stationary wing at a velocity of 10 m/s. In their model, the authors used LS-DYNA wood model *MAT 161/162 and *MAT 22, and they assumed relatively higher values of Young's modulus and specific mass density for the aluminum alloy. They found that the effective plastic strain affects significantly the impact force of the wing on a stiff beam.

In the case of an airplane crash, the accurate impact process is very difficult to study. Numerical studies can help to verify a hypothesis generated during the crash investigation based on black boxes and other available data. We describe in this article a numerical study of the impact of a large passenger airliner (a Tupolev Tu-154M) with a birch tree. Through the simulation of this crash, we evaluated the damage to the wing considering a broad spectrum of parameters such as thickness of the structural components, velocity vector components, and various airplane configurations.

We conducted a three-point bending test of the birch to characterize the birch-tree material model. We used an artificial bird impact test into the leading edge of the wing to validate the aluminum material model. We used ANSYS CFX to simulate aerodynamic pressures on the surface of the wing. Through the integration of those pressures $P(x, y)$, the resulting overall loads present on the wing surfaces have been determined. We present in the subsequent sections the methodology and results of the simulations of the impact between an airplane wing and a birch tree using the above material models and loading conditions.

2 COMPUTATIONAL MODEL AND METHOD

2.1 Aircraft Structure and Mesh

A detailed finite element (FE) model of a full-scale Tu-154M aircraft was developed on the basis of data available from public sources. Many simplifying assumptions were made to keep the geometry simple and conservative. For example, doublers, joints, landing gears and fasteners were ignored. The development of the aircraft model was performed using HyperMesh10.0. Approximately 75,000 shell elements for each airplane wing and 3,400 shell elements for the fuselage were used to model the solid part of the airplane. Coarse mesh with 57,200 solid elements and fine mesh with 288,000 solid elements were used to model the cone shape of the birch trunk. Figure 1 shows the overall view and finite element mesh of the impact model. In this study, the coordinate Y is inverse to the gravity direction, Z is the horizontal direction pointing from the tail to the nose of the airplane, while X is a line that runs along the leading edge of the left wing. The birch tree is cone-shaped and has a diameter of 0.44 m [9] at the impact height.

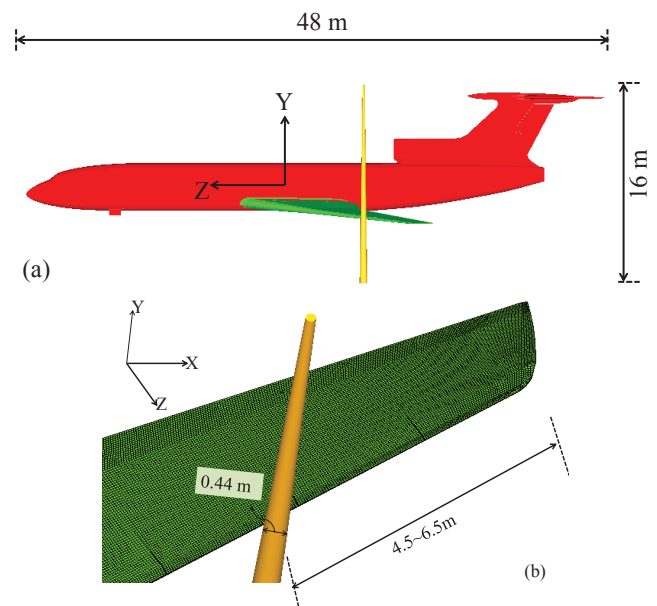


Figure 1: Overall view (a) and wing view (b) of the FEM for aircraft hit the tree

The airplane wing is a complex structure composed of spars, ribs and skin reinforced by stringers. Together, these structures form a stiff and strong box-type section [20]. The inner structure of the Tu-154M (including 41 ribs and 3 spars) and the finite element mesh of the wing are shown in Figure 2. The spars are in the form of an I-beam structure, and the ribs are thin shell structures. The thicknesses of the shell section for the spar, rib and skin may change along the wing length. Sections near

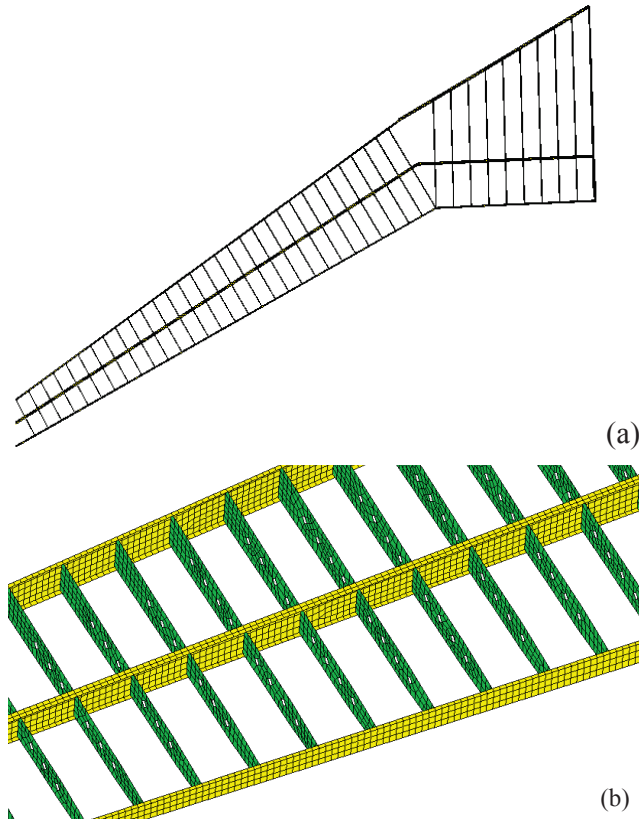


Figure 2: Inner structure and mesh of the wing

the root of the wing may be several times thicker than those at the wing tip. For example, the thicknesses of the wing skin may vary from 1.6 mm to 5 mm on the whole wing surface [6]. However, the thicknesses of the spar, rib and skin are assumed to be constant along the wing length. For parametric study, the thickness of the spar is assumed to be between 5 mm and 20 mm, the skin thickness is assumed to be between 1 mm and 5 mm, while the thickness of the ribs is assumed to be 3 mm based on knowledge of the aircraft structure and considering that the stringers, joints and bolts have been ignored.

2.2 Material Models The whole plane structure was assumed to be a V95 aluminum wrought alloy modeled with shell elements. The birch was assumed to be an orthotropic material modeled with solid elements. Section type #16 (***Fully Integrated Shell Element**) was selected for the shell section to avoid loss of energy caused by hourglass. Concentrated masses were placed uniformly inside the wings to represent 8,000 kg of fuel. The total weight of the model is 87,000 kg, matching the estimated weight of the aircraft. Two material formulations were chosen for the airplane: one is a piece-wise

plasticity isotropic material model (***MAT_24**) with an ultimate failure strain of 14%, and the other is nonlinear rate-dependent Johnson Cook model (***MAT_15**) [8]. The material parameters for the models are presented in Tables 1 and 2.

Table 1: Input of piece-wise plasticity aluminum alloy model

| Young's modulus (MPa) | Yield stress (MPa) | Tangential modulus (MPa) | Poisson's ratio | Density (kg/m ³) |
|-----------------------|--------------------|--------------------------|-----------------|------------------------------|
| 74000 | 444 | 573.8 | 0.33 | 2850 |

Table 2: Input of Johnson-Cook aluminum alloy models

| Young's modulus (MPa) | Shear modulus (MPa) | Poisson's ratio | Density (kg/m ³) |
|-----------------------|--------------------------------|---------------------------|------------------------------|
| 68900 | 25910 | 0.33 | 2700 |
| Yield stress (MPa) | Strain hardening modulus (MPa) | Strain hardening exponent | Strain rate coefficient |
| 324 | 114 | 0.4 | 0.002 |

The stress strain curves for the two material models are illustrated in Figure 3. The Johnson-Cook model shows a lower strength value but a higher failure strain. The performance of these two different material models will be discussed further under impact simulation.

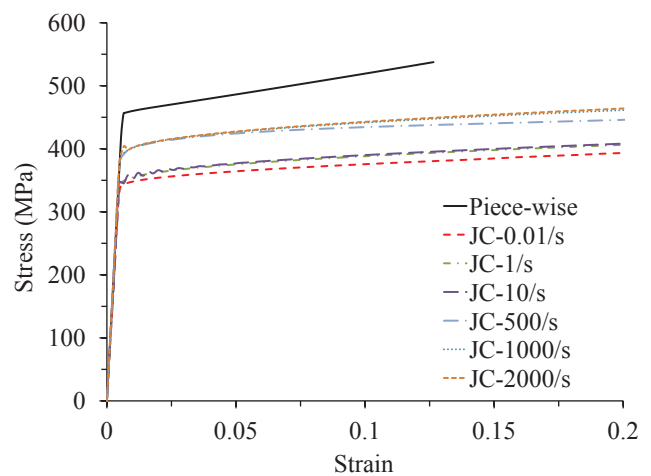


Figure 3: Differences of two material models for the aluminum alloy

Wood may be described as orthotropic elastic material (***MAT_2**) [7]. It has unique and independent me-

chanical properties in the directions of three mutually perpendicular axes: longitudinal, radial and tangential, as shown in Figure 4. The longitudinal direction, also known as the grain direction, is parallel to the fiber; the radial axis is normal to the growth ring; and the tangential axis is perpendicular to the grain but tangent to the growth rings. Considering the cone geometry of the birch, ***AOPT=4.0** was used to describe the birch as an local orthotropic material in a cylindrical coordinate system. Solid section type #1 (***Constant Stress Solid Element**) with hour glass control type #6 (***Belytschko-Bindeman Strain Co-rotational Stiffness Form**) was used for the birch solid elements. Data from public sources [12] were used to set mechanical properties of the birch, as shown in Table 3. The density value is obtained from testing of the birch lumber. The failure of the birch is determined based on a simple criterion:

$$\varepsilon_1 \geq \varepsilon_{max} \quad (1)$$

where ε_1 is the maximum effective strain and ε_{max} is the effective strain at failure. The card ***Add Erosion** was included to define the failure of the birch in which the failure effective strain has been chosen as 5%.

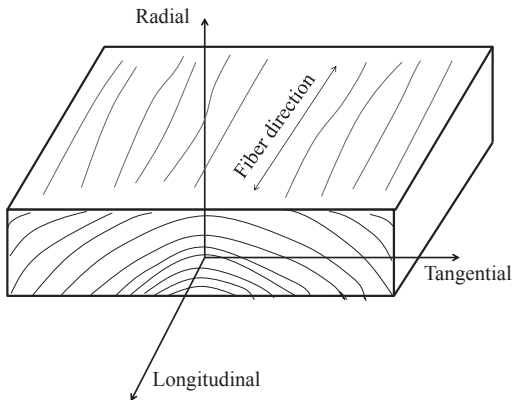


Figure 4: Three principal axes of wood

The wood model ***MAT_143** in LS-DYNA (henceforth referred to as Mat143) was primarily developed to simulate the deformation and failure of wooden guardrail posts impacted by vehicles [16]. The failure criterion of this wood model uses modified Hashin criterion, which contains tension, compression and shear in parallel and perpendicular modes. The advantages of this model include rate dependent strength and yielding with associated plastic flow. This transversely isotropic material model was characterized based on three-point bending test results, with the parameters shown in Table 4. The stress strain curves of these two material models are compared in Figure 5. In this figure, it can be seen that the two models show completely different behavior.

One is linear elastic and the other has a large range of nonlinear plasticity and strain rate dependence.

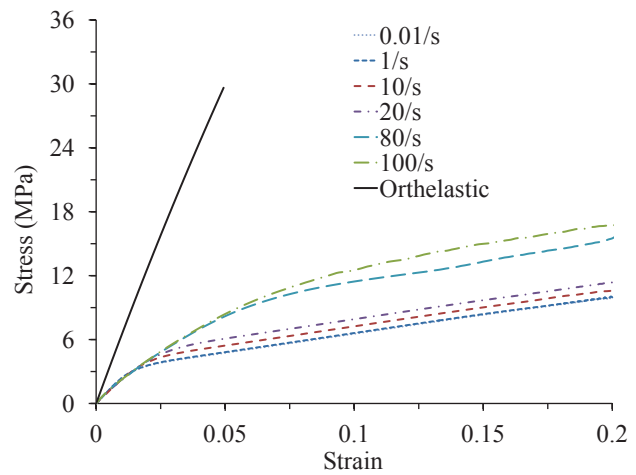


Figure 5: Differences of two material models for the wood

2.3 Selection of Contact Type As the impact with the birch tree occurs at the left wing, the fuselage and the right wing were considered as rigid bodies to increase computational efficiency. Since the right wing and fuselage are far away from the impact location, this assumption will not affect the impact failure behavior of the left wing. In LS-DYNA, for a connection between rigid bodies and a deformable body, it is recommended to use ***Constrained**. So in this model ***Constrained Extra Nodes Set** was applied to connect the fuselage and the left wing, and ***Constrained Rigid Bodies** was used to connect the right wing with the fuselage. Also in the wing structure, the spar built in the form of an I-beam contained web and flange shell elements. Connections are needed to attach the spar flange to the skin. Thus, ***Tied Surface to Surface** contact was defined to connect the spar flange and the wing skin.

For the impact process, ***Automatic Surface to Surface** card was chosen. This contact is defined for the three wing components (skin, spars, and ribs) and the birch tree. As the surface of the birch is approximately circular, **SOFT=2** (Pinball segment based contact) was implemented for more stable computations. To avoid any material penetration, ***Automatic Surface to Surface** (No soft) was also defined between the skin and spar elements.

3 VALIDATION OF MATERIAL MODELS

To make the numerical studies convincing, it was important to validate the wood and aluminum alloy material models. For the wood, a three-point bending exper-

Table 3: Material parameters for orthotropic elastic wood model

| Young's Modulus (MPa) | | | Poisson's Ratio | | | Shear Modulus (MPa) | | | Density (kg/m ³) |
|-----------------------|-------|-------|-----------------|------------|------------|---------------------|----------|----------|------------------------------|
| E_L | E_R | E_T | ν_{LT} | ν_{RL} | ν_{RT} | G_{TL} | G_{LR} | G_{RT} | |
| 10300 | 803.4 | 515 | 0.451 | 0.043 | 0.697 | 700.4 | 762.2 | 175.1 | 700 |

Table 4: Material parameters for LS-DYNA Mat143 wood model

| Parallel modulus (MPa) | Perpendicular modulus (MPa) | Parallel shear modulus (MPa) | Perpendicular modulus (MPa) | Parallel Poisson's ratio | Density (kg/m ³) |
|---------------------------------|-------------------------------------|--------------------------------------|------------------------------------------|-------------------------------|------------------------------------|
| 11400 | 243 | 588 | 87 | 0.39 | 700 |
| Parallel tension strength (MPa) | Parallel compression strength (MPa) | Perpendicular tension strength (MPa) | Perpendicular compression strength (MPa) | Parallel shear strength (MPa) | Perpendicular shear strength (MPa) |
| 35.9 | 3.59E+07 | 3.45 | 3.75 | 9.9 | 14 |

iment was conducted, producing the load and deflection curves. This curve was compared with the numerical bending simulation results, and it proved the applicability of the wood material models. In order to validate the piece-wise plasticity and Johnson-Cook model, it was necessary to evaluate the usability of this material model on the application of other aerospace impact problems, such as a bird strike conducted in the lab. The numerical results matched well with experimental results.

3.1 Leading-edge Bird Strike Analysis A bird strike is a significant threat to an aircraft, as a collision with a bird during flight may lead to serious structural damage. The leading edge of the wing is one forward facing component that is frequently studied for bird strike crashworthiness. A series of leading edge bird strike experiments [24] were conducted at Northwestern Polytechnical University in China. Based on the experimental results, a finite element model in LS-DYNA was built to simulate the impact process and failure behavior. The results were then compared with the experimental and original simulation results.

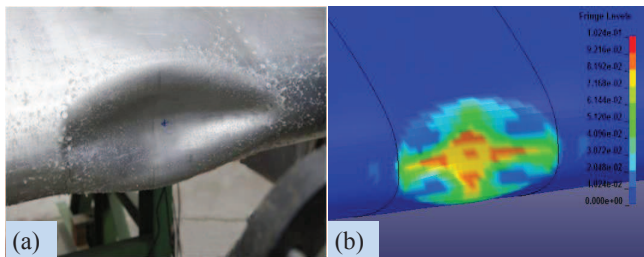


Figure 6: Experimental (a) and numerical (b) results of the deformed shape after impact

In this experiment, the leading edge was tied to a fixed supporting construction. The leading edge consisted of

skin and 4 ribs. The gas gun was positioned in front of the sample with the muzzle pointing directly at the geometric center of the leading edge structure. The projectile was a 100 mm long gelatin cylinder with a diameter of 50 mm. The density of the gelatin was 1020 kg/m³. At a velocity of 153 m/s, the leading edge was not penetrated but developed a symmetric deformation area as shown in Figure 6 (a). The displacement of the middle rib was recorded using a displacement sensor whose location is shown in Figure 7.

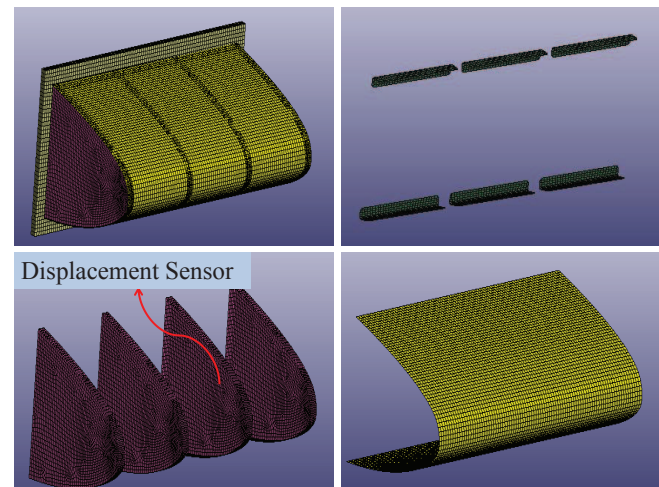


Figure 7: Components and finite element mesh of the leading edge structure

The finite element model of the leading edge structure is shown in Figure 7. The structure is built up with ribs, skin and attachments designed to tie the skin and the supporting frame together. The entire finite element model of the leading edge consists of 37,844 elements, including 21,034 shell elements (leading edge),

5,022 Smooth Particle Hydro-dynamic (SPH) elements (projectile) and 7,648 solid elements (supporting frame). SPH is a powerful mesh free method and is considered to be the most efficient, experimentally validated for simulating a liquid-like material [10]. It was widely accepted to simulate the events related to bird strikes [13, 14].

Two kinds of contact definitions are used in the simulation. One is ***Automatic Nodes to Surface** between the projectile and the leading edge, the other one is ***Tied Surface to Surface** between each attached component of the leading edge structure. The piece-wise plasticity material mathematical representation was applied to the leading edge structure. For the steel supporting construction, an elastic-plastic material model was assigned.

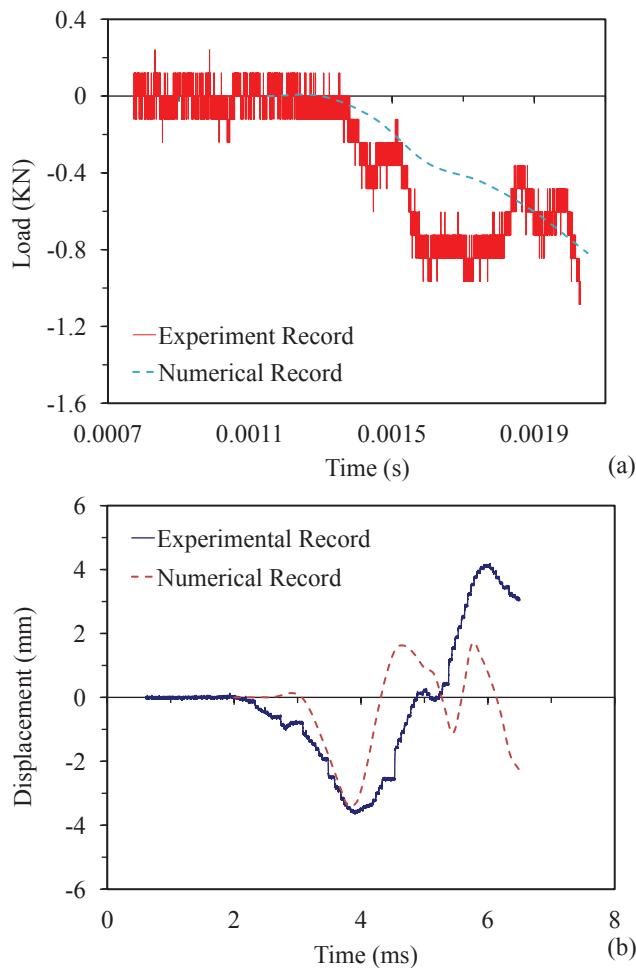


Figure 8: Experimental and numerical results of the load (a) and displacement (b) history

Figure 6 shows the experimental and simulation results of the bird strike into the leading edge. The simulation contour captures the failure area fairly well. The plastic deformation expanded symmetrically and was

constrained in the horizontal direction by the ribs. The load history at the fix point and the displacement history of the rib were also recorded and were compared with experimental data (as shown in Figure 8). The simulation results follow the experimental trend reasonably well. However, the displacement history matches the first peak value perfectly.

3.2 Wood Bending Test and Modeling The wood three-point bending test was conducted to characterize the wood models. Using the ASTM standard D143 with some modifications based on the experimental conditions, the test was set up as shown in Figure 9 (a), with a loading span of 12 inches (304 mm). The dimension of the specimen was 25 by 25 by 410 mm with density of 698 kg/m³. The load was applied continuously throughout the test at a rate of motion of the moveable crosshead of 1.3 mm/min, and the force was recorded every second. In the simulation work, the bearing cylinders were modeled using ***Rigid Wall** in LS-DYNA. In Figure 9 (b), the white circles indicate the rigid walls in the simulation.

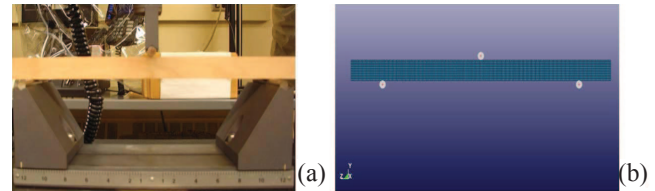


Figure 9: Set up of three-point bending test: (a) experiment (b) simulation

The load was plotted against deflection curves as shown in Figure 10. The experimental and Mat143 curves show almost identical non-linear behavior while the orthotropic elastic model show linear behavior. The results indicate that the real wood may display some softening behavior during the loading process. Fracture energy of the wood described by the linear model (green line) is almost four times larger than the energy produced in both the experiment (blue line) and Mat143 simulation (red line). A live birch tree is not dry; a living tree will be softer and weaker than the dry wood used in the three-point bending test. Hence, the simulation results produced using the selected dry-wood models are conservative. Morka et al. [15] also performed a three-point bending experiment, but their parameters for the birch tree are slightly different.

4 EVALUATION OF AIRCRAFT IMPACT WITH THE TREE

4.1 Preliminary Prediction One of the simple theories for impact assessment is the solidity ratio, which

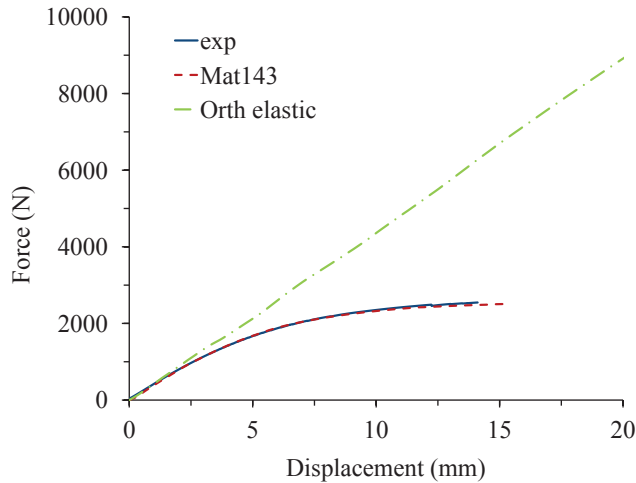


Figure 10: Load vs. deflection curves of the modeling and experimental results

can be used to estimate the crash resistance between two colliding bodies. The structure with the higher solidity ratio is considered to cut through the one with the lower solidity ratio without being damaged. The solidity ratio, ρ , is defined as the ratio of structural mass M divided by enclosed structural volume V .

The structural volume is the volume enclosed by the outer periphery, not including the material volume. This value can be obtained from LS-DYNA model geometry. Taking an estimated mass $M_{wing}=21500$ kg and volume $V_{wing}=23.65$ m³, the solidity ratio of the wing is $\rho_{wing}=930$ kg/m³. For the solid birch, the solidity ratio is equivalent to its density, 700 kg/m³. According to the above factors, the wing should cut through the birch. During the impact of the wing into the birch, contact will mainly occur between the birch and the leading edge of the wing, or between the birch and the wing's front spar.

Next, it is necessary to consider the impact resistance of the leading edge and the spar individually. For the leading edge only, the mass is much smaller, $M_{skin}=2456.6$ kg, while the enclosed volume is the same as the wing structure, $V_{skin}=23.65$ m³. Its solidity ratio is $\rho_{wing}=104$ kg/m³, which is much smaller than the density of the birch. Thus the birch should damage the leading edge easily.

Using the same logic, the solidity ratio of the aluminum alloy spar is $\rho_{spar}=2,700$ kg/m³, a much higher density than that of the birch (700 kg/m³). Hence, the front spar should cut the birch without any difficulty. It should be noted that the solidity ratio theory can only be used as an estimation because the dynamics of the impact are not taken under consideration. An accurate determination of the strength of the wing relative to the

strength of the birch requires a detailed dynamic finite element analysis.

4.2 Results of Finite Element Analysis In finite element analysis, simulations of a wing structure hitting a birch tree are performed. The initial conditions for the airplane impact are set within the following ranges: a flight velocity from 77.7 m/s to 80 m/s in the horizontal direction (v_z) and from 0 m/s to 19.2 m/s in the vertical direction (v_y), a roll angle from 0° to 5° (left wing down), a pitch angle from 0° to 14° (upward from horizontal), and a yaw angle that is assumed to be 0°. The flight velocity was assigned to the whole aircraft nodes using ***Initial Velocity**. Impact simulations were performed in LS-DYNA using a computer with an eight-core processor. The simulation of the first 0.05 s of the time after impact took about 20 hours of computational time. To obtain a comprehensive picture of the resulting damage and a good understanding of the performance of different material models, several combinations of material models and velocity vector angles were selected for the simulations (Table 5).

Table 5: Summary of analyzed cases

| Jobs | Aluminum alloy model | Wood model | Horizontal velocity (m/s) | Vertical Velocity (m/s) |
|------|-----------------------|------------------------|---------------------------|-------------------------|
| Job1 | Piece-wise plasticity | Orthotropic elasticity | 77.7 | 19.2 |
| Job2 | Piece-wise plasticity | Orthotropic elasticity | 80 | 0 |
| Job3 | Johnson Cook | Orthotropic elasticity | 77.7 | 19.2 |
| Job4 | Piece-wise plasticity | Mat143 | 77.7 | 19.2 |
| Job5 | Johnson Cook | Mat143 | 77.7 | 19.2 |
| Job6 | Johnson Cook | Mat143 | 80 | 0 |

Based on the analysis of all the above cases, it has been observed that the damage process can be divided into two stages. During the initial stage of impact (the first 0.01 s), the leading edge skin is destroyed by the birch and all shell elements of the leading edge skin contacted by the birch have failed. It is also found that only a few solid elements of the birch failed before the contact with the spar. Then after contacting with the spar (0.01

to 0.022 s), the solid elements of the birch failed gradually while no failure was observed for the spar elements. Reviewing the plastic strain history, it was found that most of the spar elements were in elastic range while the maximum plastic strain was only 0.025. These results agree with the preliminary predictions. The leading edge skin displayed little impact resistance while the spar is very strong and survives the impact load.

In summary, for every investigated vector velocity, for every used mesh, for every combination of considered material models, and for every configuration of the airplane, the left wing of the airplane cuts the birch tree into two parts. The upper part of the birch receives an impulse that forces the tree to fall in the direction opposite to the motion of the airplane.

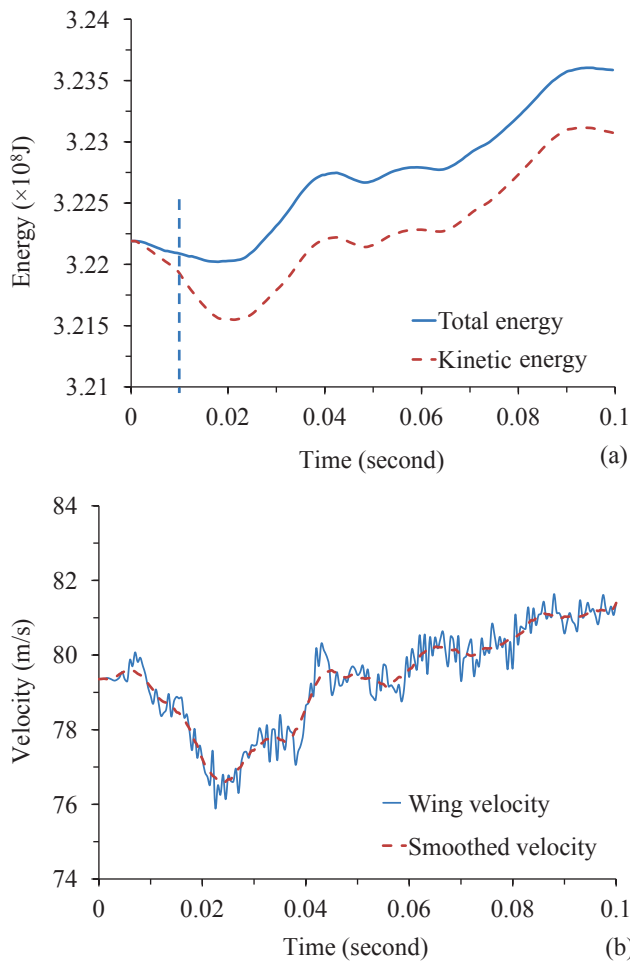


Figure 11: Energy (a) and velocity (b) history during the whole impact process

The energy and velocity histories for the impact are plotted in Figure 11. The node at the tip of the left wing was selected to record the velocity history. The energy plot shows an obvious decrease in kinetic energy

(red dashed line) for the first 0.022 s, which indicates that elastic deformation of the wing structure occurred during impact. The small decrease in total energy (blue line) was caused by the dissipation of energy during the impact in the form of sliding energy. After the birch tree was cut off, no energy dissipation occurred. As shown by the energy plot, both the kinetic and total energies are proportional. The subsequent increase of the energies is generated due to the springback process of the deformed wing.

The energy and velocity plots also demonstrate the two-stage damage process. The kinetic energy plot shows a faster decreasing rate after 0.01 s compared with the first 0.01 s. This is more obvious from the velocity plot, which shows that initially the velocity decreases slightly from 79.35 to 79 m/s during the first 0.01 s, but a steep decrease (from 79 to 76 m/s) occurs during the next 0.012 s.

The velocity of the aircraft’s tail was monitored to identify the plane’s rotation during the impact. As shown by the blue line in Figure 12 below, the tail moved to the right after the impact, which indicates that the front part of the plane moved to the left, as expected. At the same time, the vertical velocity (indicated by a red dashed line in the same figure) shows a steady linear decrease during the 0.1 s after impact.

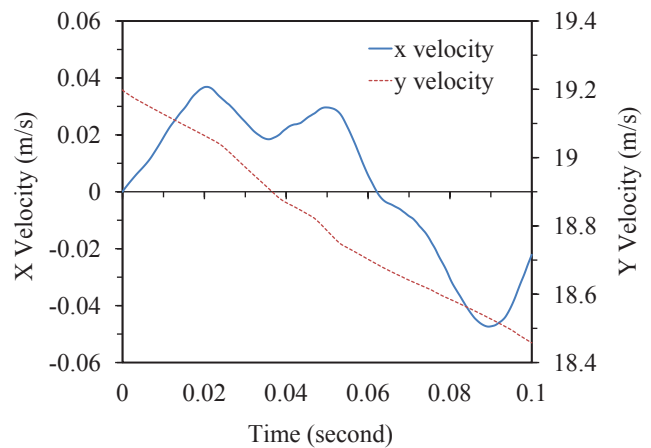


Figure 12: X and Y velocity history of the aircraft tail

The fracture energy of the wing elements calculated for different cases (listed in Table 5) were also compared in Figure 13 below. The accumulated fracture energy of the wing elements during the impact has been selected as a damage parameter measuring numerical sensitivity of the material models and mesh density for various flight configurations. In LS-DYNA, the internal energy or strain energy is computed based on the six components of the stress and strain (tensorial values). The

fracture energy was defined as the total internal energy of all the elements of the left wing.

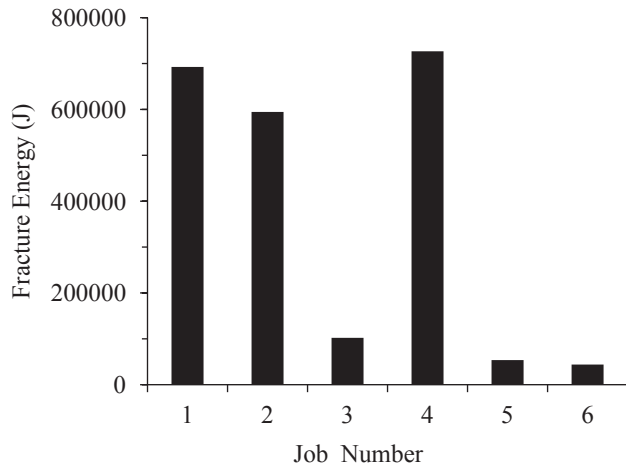


Figure 13: Fracture energy of the wing for different numerical cases from Table 5

Using the selected six cases, it has been determined that the inclined cases with a vertical velocity of 19.2 m/s accumulated more fracture energy than the horizontal cases for the same airplane configuration with the pitch angle of 14° . This difference may be due to the fact that a higher horizontal velocity will reduce the time of contact. The orthotropic elastic and Mat143 wood models display similar performance, while the Johnson-Cook model significantly lowered the fracture energy compared with the piece-wise plasticity model. However, even with different material models and various impact angles, all the cases show nearly the same results. The front spars in all cases cut the birch tree into two pieces. Since the case marked as Job4 in Table 5 produces the highest fracture energy, additional parametric studies will be shown in the following section using Job4 material model, airplane configuration, velocity vector, and mesh.

Based on conducted parametric studies of all the cases from Table 5, it was concluded that the piece-wise plasticity aluminum-alloy model and the orthotropic elastic wood model (which were used in cases Job1 and Job2) provide the most conservative combination in the impact simulation.

4.3 Parametric Study of Material Thickness in the Wing Structure To further understand how the skin and spar thickness affected the degree of wing damage, we performed a parametric study of the thickness of the skin and the spars. The relationship of velocity reduction and eroding kinetic energy against the skin thickness (ranging from 1 mm to 5 mm) were plotted in

Figure 14. The velocity reduction is defined by difference between the initial velocity and the velocity when the wing completely cuts off the birch tree. The eroding kinetic energy corresponds to the accumulative kinetic energy of the eroded skin elements. The velocity reductions for all the thicknesses of the skin are very small, indicating that the skin has small resistance to the impact. With the increasing thickness of the skin, both the velocity reduction (green line) and the eroding kinetic energy (blue line) displayed an increasing trend. The increased skin thickness slightly increases the resistance of the wing to impact. At the same time, the eroding kinetic energy increases proportionally to the increase of the skin mass. It was found that the variation of the skin thickness from 3 mm to 5 mm resulted in minimal variation in velocity reduction. Thus, increasing the thickness of the skin to 5 mm would not make a significant difference in resisting the impact.

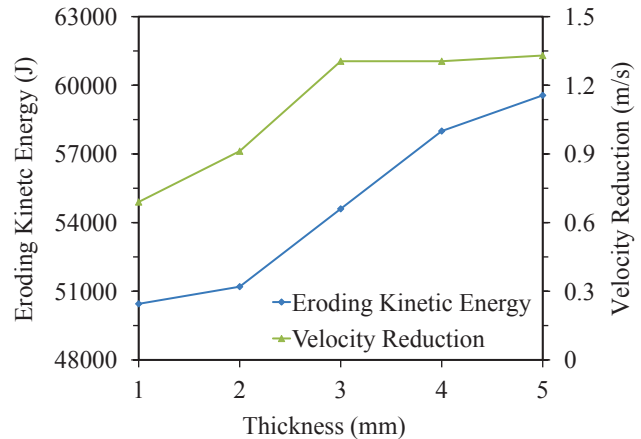


Figure 14: Resultant velocity and eroding kinetic energy against skin thickness

Figure 15 displays the final plastic strain contour of the front spar for different thicknesses (ranging from 5 mm to 20 mm) at flight velocity $v_z=77.7$ m/s and $v_y=19.2$ m/s. As the spar thickness decreases, the spar elements suffer increasing plastic deformation. The critical thickness for the spar element failure (which we define as the minimum spar thickness where no element is deleted during the impact) was found to be 8 mm, although even a 5 mm spar has not been completely bridged. As we can see, no apparent deformation was observed in Figure 15 (a), (b) and (c), and the maximum plastic strain of the elements was only 0.055, far lower than the failure strain of 0.14, as demonstrated in Figure 3 above. Even for the thickness of 5 mm, the spar clearly cuts through the birch tree without being broken. Considering that in the wing of a Tu-154M, the spar thickness is 12 mm [2], and there are two more spars

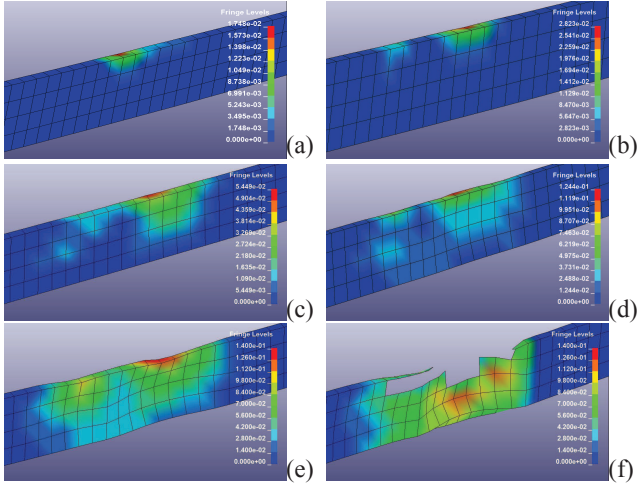


Figure 15: The final plastic strain contour of the spar with thickness of 20 mm (a), 17 mm (b), 13 mm (c), 10 mm (d), 8 mm (e) and 5 mm (f) at flight velocity $v_z=77.7$ m/s and $v_y=19.2$ m/s.

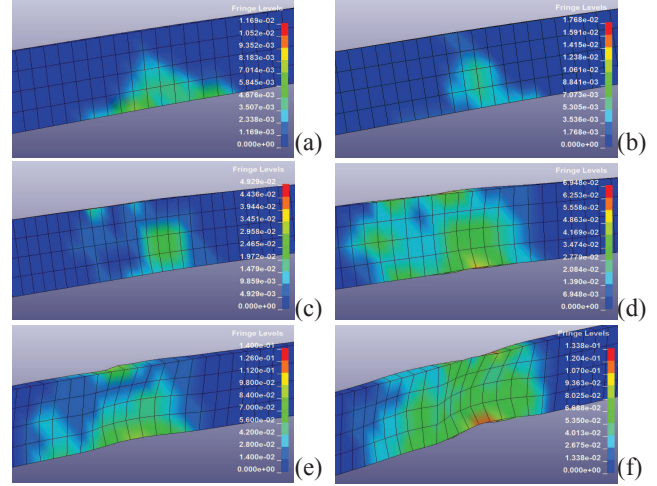


Figure 16: The final plastic strain contour of the spar with thickness of 20 mm (a), 17 mm (b), 13 mm (c), 10 mm (d), 8 mm (e) and 5 mm (f) at flight velocity $v_z=80$ m/s

behind the front spar, it can be concluded that there is enough margin of safety for the wing to survive the impact with the birch tree under consideration for every studied spar thickness and impact scenario.

It is also observed that the top flange of the spar suffers more serious damage than the bottom flange. This is due to the positive vertical velocity of the plane, which caused compression contact between the birch tree and the top flange. The final plastic strain contours of a front spar with different thicknesses (ranging from 5 mm to 20 mm) at flight velocity $v_z=80$ m/s are shown in Figure 16. Similar to the results shown in Figure 15, the spar elements suffer increasing plastic strain with the decrease of the spar thickness. In this case, the bottom flange suffers more damage because it touches the birch earlier. However, by comparing the damage for the same spar thicknesses in Figures 15 and 16, we can conclude that the case of a horizontal flying airplane produced less damage of the front spar than the cases with an inclined velocity vector ($v_z=77.7$ m/s and $v_y=19.2$ m/s).

5 AERODYNAMIC PRESSURES

During high speed flight, the pressure load produced by air flow is distributed over the airplane's external surfaces. For an accurate evaluation of the impact damage, the aerodynamic pressures need to be incorporated into the finite element model. In this section, the computational fluid dynamic method (CFD) is used to calculate aerodynamic pressure profiles.

5.1 CFD Modeling Methodology The air flow over the wing/plane profile yields a Reynolds number large enough that the resulting flow remains within the turbulent regime, meaning that the inertial forces are larger than the viscous forces. This dominance of inertial forces causes a degradation of the boundary layer due to the formation of eddies within the flow. To account for this phenomenon, determine the transient fluctuations in the resulting velocity profile, and solve the unknown Reynolds stresses within the Reynolds Averaged Navier-Stokes equations (RANS), the $k - \epsilon$ model is used [18]. The Reynolds stress is a function of the turbulence kinetic energy (k) and the eddy viscosity (μ_t). When the resulting Reynolds stress is substituted into the RANS, there are two resulting unknown terms: the effective viscosity (μ_{eff}) and the modified pressure (p').

$$\mu_{eff} = \mu + \mu_t \tag{2}$$

$$p' = p + \frac{2}{3}\rho k + \frac{2}{3}\mu_{eff}\nabla \cdot U \tag{3}$$

where ρ is fluid density and U , p and μ represent the instantaneous velocity vector, pressure and viscosity, respectively. The effective viscosity is a function of the eddy viscosity. In the $k - \epsilon$ model, the eddy viscosity is a function of the turbulence kinetic energy (k) and dissipation (ϵ),

$$\mu_t = C_\mu \rho \frac{k^2}{\epsilon} \tag{4}$$

where C_μ is a model constant. To determine the eddy viscosity and the resulting modified pressure, two additional transport equations are solved such that both the

k and ϵ are determined.

$$\frac{\partial(\rho k)}{\partial t} + \nabla \bullet (\rho U k) = \nabla \bullet \left[\left(\mu + \frac{\mu_t}{\mu_k} \right) \nabla k \right] + P_k - \rho \epsilon \quad (5)$$

$$\frac{\partial(\rho \epsilon)}{\partial t} + \nabla \bullet (\rho U \epsilon) = \nabla \bullet \left[\left(\mu + \frac{\mu_t}{\mu_\epsilon} \right) \nabla \epsilon \right] + \frac{\epsilon}{k} (C_{\epsilon 1} P_k - C_{\epsilon 2} \rho \epsilon) \quad (6)$$

where μ_k , μ_ϵ , $C_{\epsilon 1}$ and $C_{\epsilon 2}$ are all taken to be constants and P_k is defined as the turbulence production due to viscous forces. The typical method for pressure calculation utilizes a staggered grid approach to mitigate the “checker-board” type problems associated with the discretization of the pressure derivative in the momentum equations over a control volume, as discussed in [3].

5.2 CFD Model Description Numerical results are obtained using ANSYS CFX, a commercial computational engine used for multi-physics computational analysis. The program has a powerful preprocessor, ICEM, which allows the input of complicated geometries as well as a post processor CFX-Post through which results can be presented in two- or three-dimensional format. The CFX algorithm is employed to solve the full, compressible Navier-Stokes equations in a Cartesian system of coordinates, using body-fitted coordinates. The solution domain is divided into many cells called control volumes. Using a finite volume approach, the differential equations are turned into a system of algebraic equations. They are numerically integrated over each of the computational cells, using a collocated cell-centered variable arrangement, where all dependent variables and material properties at the cell’s center are stored. For the momentum equations, a high resolution scheme is used that utilizes a combination of a first- and second-order upwind scheme. For pressure calculations, ANSYS uses a pressure-velocity coupling that allows the Navier-Stokes equations to be solved in a coupled manner. This procedure is similar to the SIMPLEC scheme used in CFD-ACE+ and Fluent, which was originally proposed by both Van Doormal and Raithby [19] and later enhanced by Patankar and Spalding [17]. For SIMPLEC, the equation for pressure correction is obtained from the continuity equation, and the scheme of velocity and pressure calculations is fundamentally iterative in nature.

The fluid used throughout the numerical endeavor utilized air as an ideal gas for this steady, compressible, isothermal model. The resulting isothermal condition allows for calculation of the air density. Implementation

of the plane geometry and the subsequent wing profiles into the ANSYS pre-processor required boundary conditions similar to those shown in Figure 17. The figure illustrates how the fluid domain was defined with respect to the plane/wing geometry. The front and bottom of the rectangular domain were prescribed as inlet boundary conditions that allow for x and y components of velocity to be prescribed. Figure 17 shows the resulting components of the velocity vector, which yield an attack angle assumed to be between 0° and 20° with respect to the horizontal position of the wing. The top and end of the fluid domain were set to an outlet boundary condition. The outlet was prescribed with the same mass flow as that of the inlet condition. In addition, since this numerical work is to simulate a plane or portion of a plane in flight, the side walls of the domain were set to a no-shear boundary condition. The gridding of the domain utilized an unstructured mesh, where the density of elements near the wing/plane geometry increased. This increase in elements is required in order to accurately define the flow near and around the wing, in order to capture the development of the boundary layer and the eventual separation of the boundary layer as the angle of attack increases. The resulting unstructured arrangement produced approximately 200,000 to 400,000 elements.

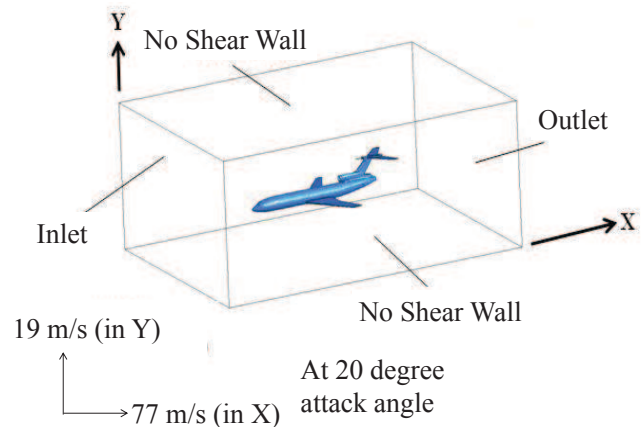


Figure 17: Overview of the boundary conditions used for the simulation of the wing/plane with the corresponding x and y component of velocity for an attack angle of 20°

To verify that there are a sufficient number of elements to accurately calculate the flow and pressures with the fluid domain, a grid convergence test was performed. This grid convergence increased the total number of elements by 25 percent and compared u , v and w velocities and pressures for various locations. ANSYS uses absolute convergence criteria, which for the pressure field typically requires convergence of the residual on the order of 1.0×10^{-4} . For cases considered here, a conver-

gence criterion of 1.0×10^{-4} was used for each of the primitive variables (u , v , w , and p).

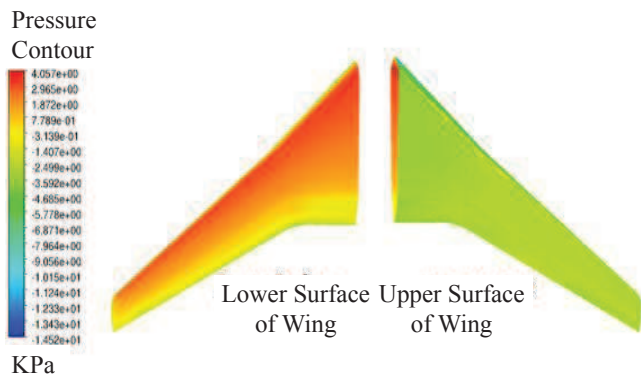


Figure 18: Super-imposed pressure contours on the lower and upper surface of the right wing profile for an attack angle of 20°

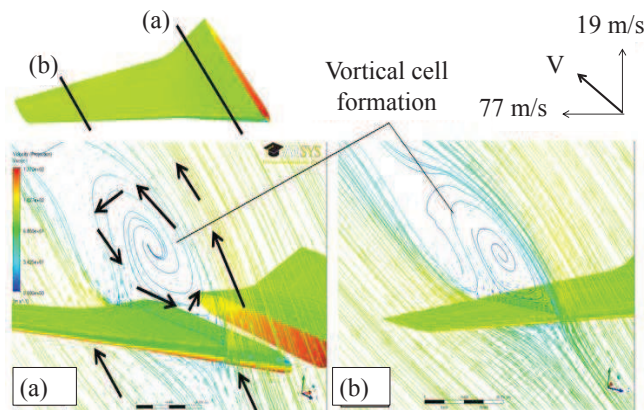


Figure 19: 2-D vectors and streamline velocity plots for an attack angle of 20° on two line sections of the wing: (a) close to the fuselage, (b) far from the fuselage.

5.3 CFD Simulation Results Figure 18 presents the results of the pressures generated on the lower and upper surfaces of the left wing for an attack angle of 20° . It can be seen that the pressure distribution on the upper surface of the wing yields lower pressures, while larger pressures are generated on the lower surface of the wing. This difference in pressure is the lift force. The upper portion of the wing near the front edge yields even lower pressures than those on the rest of the wing. This lower pressure region is due to large velocity gradients being generated from the velocity of the air with respect to the front edge of the wing wall. These large velocities cause an overall decrease in pressure due to the Bernoulli Effect.

Figure 19 presents both two-dimensional superimposed velocity vectors and velocity stream lines on two sections of the left wing surface for a 20° angle of attack. Figure 19(a) highlights the formation of the vortical cell displayed on a two-dimensional plane close to the fuselage. This vortical cell is produced as a result of large velocity and separation of the boundary layer. Consequently, the air can travel backwards or towards the front edge of the wing because of the boundary layer separation. Typically, the formation of such cells results in lower pressure regions developing on the upper portion of the wing, as shown in Figure 18. Similar velocity profiles and vortical cell formations over another two-dimensional plane located far from the fuselage are shown in Figure 19(b).

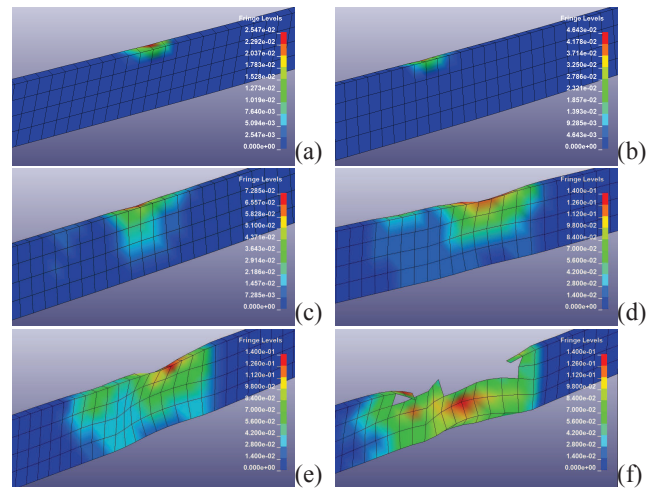


Figure 20: The final plastic strain contour of the spar with thickness of 20 mm (a), 17 mm (b), 13 mm (c), 10 mm (d), 8 mm (e) and 5 mm (f) included aerodynamic pressures loads.

5.4 FEM Analysis with the Aerodynamic Effects The pressure profiles generated by CFD for the aircraft wing top and bottom surfaces were transferred into the FEM model as surface pressure loads. Impact simulations were conducted to evaluate the influence of the aerodynamic pressure loads on spars of selected thicknesses shown in Figure 15. As shown in Figure 20, identical tendency is observed as compared to the cases without aerodynamic pressure, but the maximum plastic strain of the structure is found to be slightly higher. Also, the critical spar thickness can be assumed to be 10 mm, although even for a 5-mm thickness, the spar has not been fully bridged even for the worst damage producing case. These results indicate that the aerodynamic pressures are supported by the entire wing struc-

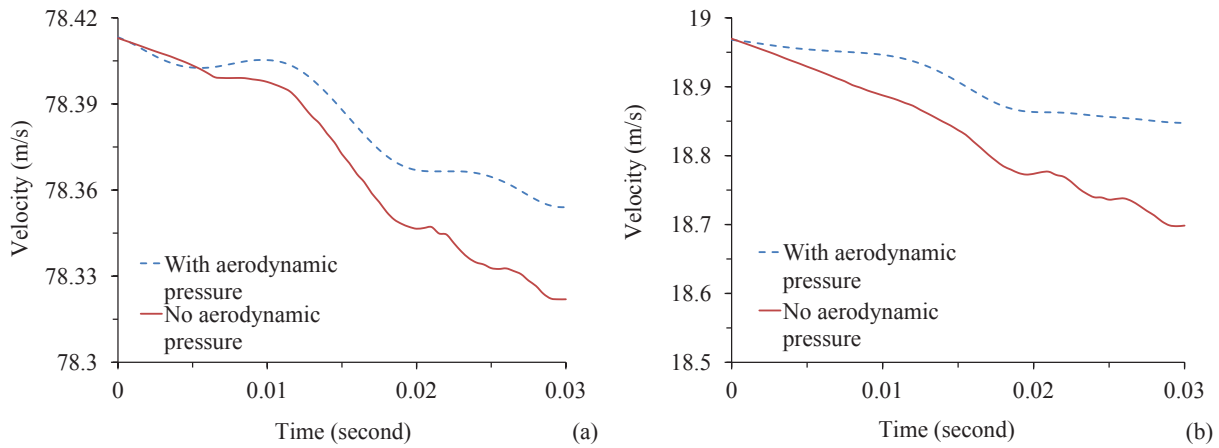


Figure 21: Comparison of resultant velocity (a) and vertical velocity (b) histories of the airplane with and without consideration of aerodynamic pressure

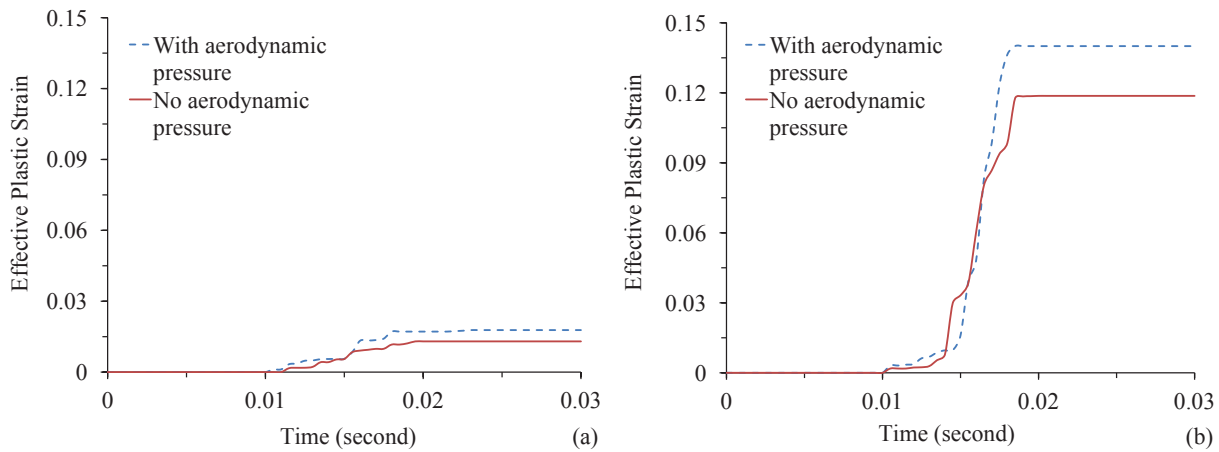


Figure 22: Effective plastic strain histories of spar (a) bottom flange elements and (b) top flange elements

ture and only slightly increased damage is observed in the front spar.

The velocity histories of the airplane with and without aerodynamic pressure are presented in Figure 21. The slightly higher vertical and resultant velocity matches with the aerodynamic effect when the airplane is flying upward, therefore proving the accuracy of the model.

For the I-beam structure, when impact occurs, the flanges are assumed to suffer normal stress while the web fails by shear stress. When the airplane flies upward, it has a vertical velocity, the top flange of the spar is compressed, and the bottom flange suffers mainly tension stresses. The effective plastic strain histories of the spar elements with a spar thickness 10 mm were also recorded, as shown in Figure 22. The top flange of the spar is damaged more seriously compared with the bottom flange. It is found that aerodynamic pressure causes higher effective plastic strain. For cases with

aerodynamic pressures (blue dashed line) and without aerodynamic pressure (red line), the plastic strains increase almost at the same time for the bottom and top flanges, as shown in both plots. Also, the effective plastic strains in both plots become constant at about 0.019 s after impact for both top and bottom elements. This result indicates that the aerodynamic pressure has no significant influence on the impact damage process.

The aerodynamic evaluation of the pressure distribution further corroborates the corresponding finite element analysis of pressure loads such that even a 5-mm thick spar would be able to withstand the impact and cut through the analyzed birch tree while the wing structure would retain its function.

6 CONCLUSIONS

1. An elastic-plastic dynamic finite element model for the impact of the aircraft wing with the birch tree was established. The numerical simulation was solved using nonlinear explicit FE code LSDYNA. The numerical results indicate that during impact, the leading edge of the wing is damaged over the length of 60–80 cm but the front spar cuts the birch into two pieces. The upper part of the birch should fall parallel to the direction of the airplane flight, which is consistent with the results of the experiment conducted with a Lockheed Constellation airplane [5].
2. The leading edge bird strike simulations were conducted using the piece-wise aluminum alloy model, and the three-point bending of the birch tree was tested and compared with the wood models. All the material behavior simulation results are in good agreement with the experiments, indicating that the material models are well characterized.
3. Parametric studies were performed to (i) analyze how the thickness of the skin and the spar in the wing structure influences the degree of damage and (ii) investigate the critical thickness for the spar failure. The results are shown qualitatively and quantitatively. The spar thickness has been shown to be responsible for the crashworthiness of the wings.
4. Aerodynamic pressure profiles were calculated by ANSYS CFX, and the numerical results contained both velocity profiles and pressure contours over the wing/plane surfaces. The effects of aerodynamic pressure on impact behavior were investigated. It has been shown that the impact damage process is not significantly affected by the pressure loads, and plastic deformations are only slightly increased in some spar elements.
5. This study explored the potential ability of numerical simulation methods in crashworthiness studies of aircraft crash investigations. The FE simulation results successfully reproduced the aircraft impact scenario, and they may provide additional guidelines and insights for aircraft design.

ACKNOWLEDGEMENTS

The authors would like to thank the four anonymous reviewers for their constructive suggestions and comments on the earlier version of this manuscript.

REFERENCES

- [1] Abboud, N., M. Levy, D. Tennant, J. Mould, H. Levine, S. King, C. Ekwueme, A. Jain, and G. Hart. 2003. Anatomy of a disaster: A structural investigation of the World Trade Center collapses. ASCE 3rd Forensic Congress, San Diego, California.
- [2] Andryukhin, W.A., W.W. Efimov and N.B. Behtina. 2003. Construction and Strength of Airplanes. Ministry of Transportation of Russian Federation. Moscow State Technical University of Civil Aviation. Moscow. http://storage.mstuca.ru/bitstream/123456789/1349/1/_doc
- [3] ANSYS, Inc. 2010. *ANSYS CFX-Solver Theory Guide*, Release 13.0 Canonsburg, Pennsylvania. http://www1.ansys.com/customer/content/documentation/130/cfx_thry.pdf
- [4] Bazant, Z.P., and Y. Zhou. 2002. Why did the World Trade Center collapse? Simple analysis. *Journal of Engineering Mechanical*. 128(1): 2-6.
- [5] Bocchieri R.T., R.M. MacNeill, C.N. Northrup, and D.S. Dierdorf. 2012. Crash simulation of transport aircraft for predicting fuel release: First phase-simulation of the Lockheed Constellation model L-1649 full-scale crash test. DOT/FAA/TC-12/43. US Department of Transportation, Federal Aviation Administration, Atlantic City International Airport, New Jersey.
- [6] Boeing 737-800 structural repair manual.
- [7] Buchar, J., S. Rolc, J. Lisy, and J. Schwengmeier. 2001. Model of the wood response to the high velocity of loading. Proceedings of the 19th International Symposium of Ballistics, Interlaken, Switzerland. <http://www.mif.pg.gda.pl/kft/Akron1/wood%20-model%20orthropical%20elastic.pdf>
- [8] Buyuk, M., S. Kan, and M. Loikkanen. 2009. Explicit finite-element analysis of 2012-T3/T351 aluminum material under impact loading for airplane engine containment and fragment shielding. *Journal of Aerospace Engineering* 22(3): 287-295.
- [9] Cieszewski, C.J., F. Antony, P. Bettinger1, J. Dahlen, R.C. Lowe, and M. Strub. 2013. Wood quality assessment of tree trunk from the tree branch sample and auxiliary data based on NIR Spectroscopy and SilviScan. *Math. Comput. For. Nat.-Res. Sci.* 5(1): 86–111. Available online at: <http://mcfns.com/index.php>. Last accessed online on Mar. 30, 2013.

- [10] Cleary, P.W., M. Prakash, J. Ha, and N. Stokes. 2007. Smooth particle hydrodynamics: Status and future potential. *Progress in Computational Fluid Dynamics, an International Journal*, 7(2): 70-90.
- [11] Final report from the examination of the aviation accident no 192/2010/11 involving the Tu-154M airplane, tail number 101, which occurred on April 10, 2010 in the area of the SMOLENSK NORTH airfield. Committee for Investigation of National Aviation Accidents, Warsaw, Poland. <http://mswia.datacenter-poland.pl/FinalReportTu-154M.pdf>
- [12] Forest Products Laboratory 2010. *Wood Handbook, Wood as an Engineering Material* General Technical Report FPL-GTR-190. United States Department of Agriculture Forest Service Madison, Wisconsin
- [13] Lavoie, M.A., A. Gakwaya, and M.N. Ensan. 2008 Application of the SPH Method for Simulation of Aerospace Structures under Impact Loading. *Proceedings of the 10th International LSDYNA Users Conference*, Dearborn, Michigan
- [14] McCarthy, M.A., J.R. Xiao, C.T. McCarthy, A. Kamoulakos, J. Ramos, J.P. Gallard, and V. Melito. 2004. Modelling of bird strike on an aircraft wing leading edge made from fibre metal laminates – Part 2: Modelling of impact with SPH bird model. *Applied Composite Materials*, 11(5): 317-340.
- [15] Moroka, A., T. Niezgodna, P. Dziewulski, and S. Stanislawek. 2012. Problems of numerical modeling of collision of bodies. Smolensk Conference, Warsaw, Poland.
- [16] Murray Y, J. Reid, R. Faller, B. Bielenberg and T. Paulsen. 2005. Evaluation of LS-DYNA wood material model 143. FHWA-HRT-04-096. US Department of Transportation, Federal Highway Administration, McLean, Virginia
- [17] Patankar, S.V., and D.B. Spalding. 1972. A calculation procedure of heat, mass and momentum transfer in three-dimensional parabolic flow. *International Journal of Heat and Mass Transfer* 15(10): 1787-1806.
- [18] Patankar, S.V. 1980. *Numerical Heat Transfer and Fluid Flow*. McGraw-Hill. New York.
- [19] Van Doormaal, J.P., and G.D. Raithby. 1984. Enhancement of the SIMPLE method for predicting incompressible fluid flows. *Numerical Heat Transfer*. 7(2): 147-163.
- [20] Virtual aircraft design: Part 4 wing (In Russian) http://cnit.ssau.ru/virt_lab/krilo/index.htm
- [21] Wierzbicki, T., and X. Teng. 2003. How the airplane wing cut through the exterior columns of the World Trade Center. *International Journal of Impact Engineering*. 28(6): 601–625.
- [22] Wierzbicki, T., L. Xue, and M. Hendry-Brogan. 2002. Aircraft impact damage. In E. Kausel, (Ed.) *The Towers Lost and Beyond* (pp. 31-64). Massachusetts Institute of Technology, Cambridge, Massachusetts. <http://web.mit.edu/civenv/wtc/Towers%20Lost%20&%20Beyond.pdf>
- [23] Xue, L., L. Zheng, and T. Wierzbicki. 2003. Interactive failure in high velocity impact of two box beams. ASME 2003 International Mechanical Engineering Congress and Exposition, Washington, DC, USA.
- [24] Zhao MY., and J. Li. 2011. Efficiency metallic leading edge structure bird strike resistance design *Advanced Materials Research* 338(84):84-89.